



# 1 Rapid fragmentation of Thwaites Eastern Ice Shelf, West 2 Antarctica

3

4 Douglas I. Benn<sup>1</sup>, Adrian Luckman<sup>2</sup>, Jan A. Åström<sup>3</sup>, Anna J. Crawford<sup>1</sup>, Stephen L.  
5 Cornford<sup>2</sup>, Suzanne Bevan<sup>2</sup>, Rupert Gladstone<sup>4</sup>, Thomas Zwinger<sup>3</sup>, Karen Alley<sup>5</sup>, Erin Pettit<sup>6</sup>  
6 and Jeremy Bassis<sup>7</sup>

7

8 <sup>1</sup>School of Geography and Sustainable Development, University of St Andrews, St Andrews,  
9 KY16 9AL, UK

10 <sup>2</sup>Department of Geography, Swansea University, Swansea, SA2 8PP, UK

11 <sup>3</sup>CSC-IT Center for Science, FI-02101 Espoo, Finland

12 <sup>4</sup>The Arctic Centre, University of Lapland, 96101 Rovaniemi, Finland

13 <sup>5</sup>Department of Environment and Geography, University of Manitoba, Winnipeg, MB R3T  
14 2M6, Canada

15 <sup>6</sup>College of Earth, Ocean and Atmospheric Sciences, Oregon State University, Corvallis, OR  
16 97331-5503, USA

17 <sup>7</sup>Department of Earth and Environmental Sciences, University of Michigan, Ann Arbor, MI  
18 48109-1005, USA

19

20 *Correspondence to:* Doug Benn (dib2@st-andrews.ac.uk)

21

22 **Abstract** Ice shelves play a key role in the dynamics of marine ice sheets, by buttressing  
23 grounded ice and limiting rates of ice flux to the oceans. In response to recent climatic and  
24 oceanic change, ice shelves fringing the West Antarctic Ice Sheet (WAIS) have begun to  
25 fragment and retreat, with major implications for ice sheet stability. Here, we focus on the  
26 Thwaites Eastern Ice Shelf (TEIS), the remaining pinned floating extension of Thwaites  
27 Glacier. We show that TEIS has undergone a process of fragmentation in the last five years,  
28 including brittle failure along a major shear zone, formation of tensile cracks on the main  
29 body of the shelf, and release of tabular bergs on both eastern and western flanks.  
30 Simulations with the Helsinki Discrete Element Model (HiDEM) show that this pattern of  
31 failure is associated with high backstress from a submarine pinning point at the distal edge of  
32 the shelf. We show that a significant zone of shear upstream of the main pinning point  
33 developed in response to the rapid acceleration of the shelf between 2002 and 2006, seeding  
34 damage on the shelf. Subsequently, basal melting and positive feedbacks between damage  
35 and strain rates weakened TEIS, allowing damage to accumulate. Thus, although backstress  
36 on TEIS has likely diminished through time as the pinning point has shrunk, accumulation of  
37 damage has ensured that the ice in the shear zone has remained the weakest link in the  
38 system. Experiments with the BISICLES ice sheet model indicate that additional damage to  
39 or unpinning of TEIS are unlikely to trigger significantly increased ice loss from WAIS, but the  
40 calving response to loss of TEIS remains highly uncertain. It is widely recognised that ice-  
41 shelf fragmentation and collapse can be triggered by hydrofracturing and/or unpinning from  
42 ice shelf margins or grounding points. Our results indicate a third mechanism, *backstress-*  
43 *triggered failure*, that can occur when ice fractures in response to stresses associated with  
44 pinning points. In most circumstances, pinning points are essential for ice shelf stability, but  
45 as ice shelves thin and weaken the concentration of backstress in damaged ice upstream of  
46 a pinning point may provide the seeds of their demise.

47

48

49



## 50 1. Introduction

51

52 Ice shelves play a key role in the dynamics of marine ice sheets. By transmitting resistive  
53 stresses from lateral or basal pinning points to the grounding line, ice shelves buttress  
54 grounded portions of the ice sheet and constrain ice flow (e.g. Doake et al., 1998; DuPont  
55 and Alley, 2005). If buttressing is reduced or lost following the retreat or disintegration of ice  
56 shelves, tributary glaciers can accelerate and increase ice flux to the ocean (Scambos et al.,  
57 2004). Accelerated ice discharge may be temporary and reversible, but modelling studies  
58 indicate that in some circumstances (e.g. where the bed is steeply retrograde) ice-shelf  
59 break-up may initiate sustained loss of grounded ice and irreversible retreat through the  
60 marine ice sheet and marine ice cliff instabilities (Schoof, 2012; Sun et al., 2020; DeConto et  
61 al., 2021; Bassis et al., 2021). Large areas of the West Antarctic Ice Sheet are vulnerable to  
62 this process, particularly Thwaites Glacier and Pine Island Glacier in the Amundsen Sea  
63 Sector (Scambos et al., 2017).

64

65 In response to recent climatic and oceanic change, the geographical extent of ice shelf  
66 retreat and disintegration has spread southward from the Antarctic Peninsula into West  
67 Antarctica (Cook and Vaughan, 2010; Liu et al., 2015). If the response of WAIS to a range of  
68 climate change scenarios is to be predicted with confidence, understanding the processes  
69 affecting ice shelf stability is a matter of urgency (Fox-Kemper et al., 2021). The prominent  
70 role of melt pond drainage and hydrofracturing in the demise of Larsen B in 2002 (Scambos  
71 et al., 2003) has focused attention on surface melting as a trigger for ice-shelf disintegration  
72 (e.g. Robel and Banwell, 2019; Lai et al., 2020). Recent observations, however, indicate that  
73 ice-shelf retreat and disintegration can occur in the absence of surface melt, if basal melting  
74 causes ice to lose contact with lateral or sea-floor pinning points. Examples include major  
75 rifting and calving from Pine Island Glacier following weakening of lateral pinning points  
76 (Arndt et al., 2018; Lhermitte et al., 2020) and fragmentation of the Thwaites Western Ice  
77 Tongue (TWIT; Fig. 1) following progressive loss of a sea-floor pinning point (Tinto and Bell,  
78 2011; Miles et al., 2020).

79

80 In this paper, we focus on the Thwaites Eastern Ice Shelf (TEIS), the remaining pinned  
81 floating extension of Thwaites Glacier. TEIS is currently pinned at its distal end by a sea-floor  
82 ridge (Fig. 1), but rates of ice thinning over this pinning point suggest that complete unpinning  
83 could occur in less than one decade (Alley et al., 2021; Wild et al. 2021). Here we use a  
84 high-frequency time series of Sentinel-1 imagery to show that within the last 5 years TEIS  
85 has transitioned from an intact ice shelf to a highly fragmented state, crossing a threshold  
86 from stable to unstable. Using the Helsinki Discrete Element Model (HiDEM), we show that  
87 this threshold-crossing behaviour was not the consequence of progressive unpinning, but  
88 occurred due to the failure of weakened ice in response to stresses associated with the  
89 pinning point. Pinning points, therefore, are not necessarily a stabilising factor for ice shelves,  
90 but instead may have a destabilising effect when ice around them is sufficiently weakened.  
91 Finally, we use the ice-sheet model BISICLES to explore the possible near-term  
92 consequences of damage evolution, shelf thinning and decoupling of TEIS from the pinning  
93 point. The recent behaviour and imminent break-up of TEIS has important implications for  
94 both ice shelf stability and the effectiveness of buttressing from intact and fragmented ice  
95 shelves.

96

97

98

99



00 **2. Methods**

01

02 **2.1 Observations**

03 We use satellite data to monitor surface features which indicate the evolution of surface and  
04 basal fractures, and to derive surface velocity fields to monitor change in ice flow rate and  
05 patterns of surface strain. The main source of satellite data is Sentinel-1 (resolution ~10m),  
06 but we also use velocity products from MODIS (Alley et al., 2021), MEaSURES (Mouginot et  
07 al., 2017) and ITS-LIVE (Gardner et al., 2019) to provide historical context.

08

09 Surface velocity fields are derived from Sentinel-1 Interferometric Wide (IW) Mode using  
10 standard feature/speckle tracking procedures (e.g. Luckman et al., 2015). We employ the  
11 whole satellite data archive since 2014 to produce individual velocity maps on key dates and  
12 mean velocity products on an annual, quarterly or monthly basis to assess the development  
13 of speed and strain. We use a combination of 6-day and 12-day Sentinel-1 image pairs from  
14 the available archive and our feature tracking window size is 416x128 which equates to ~1km  
15 in range and azimuth. We sample the velocity field at 50 x 10 pixels before geocoding to the  
16 Antarctic Polar Stereographic projection (EPSG:3031) at 100m resolution using the REMA  
17 DEM (Howat et al., 2019) gap-filled by BedMap2 surface topography data (Fretwell et al.,  
18 2013). Strain rates are derived from selected 6-day pair velocity maps with high coherence  
19 and low noise, and are calculated in a 3x3 neighbourhood for optimum resolution.

20

21 **2.2 Modelling**

22 Modelling experiments were conducted with the Helsinki Discrete Element Model (HiDEM)  
23 and the BISICLES ice sheet model, to investigate fracture processes underway at TEIS and  
24 ice-sheet dynamic response to the ice shelf's evolution, respectively.

25

26 HiDEM represents ice as arrays of particles linked by breakable elastic beams, and explicitly  
27 simulates ice fracture and calving processes (Åström et al., 2013). Particles are stacked  
28 together in a hexagonal close-packed lattice to form a 3D domain representing observed ice  
29 geometries. The version used in this study (HiDEM2.0) was developed by JAA and Fredrik  
30 Robertsen at the CSC-IT Center for Science, Finland, with data structures and parallelisation  
31 scheme optimized for effective computation. On a modern HPC system HiDEM2.0 can  
32 compute  $10^6$  timesteps for  $10^8$  particles in about 24 hours, with a timestep length of 0.001  
33 seconds. This is 1-2 orders of magnitude faster than older versions of HiDEM, allowing  
34 simulations of much larger domains with smaller particle sizes.

35

36 Five parameters determine the bulk tensile and shear strength of the ice: particle size, beam  
37 width to particle diameter ratio, beam tensile breaking strain, maximum beam endpoint  
38 bending angle, and density of randomly-distributed pre-broken beams (damage). In the  
39 simulations reported here, we use a particle size of 40m, a beam width to particle diameter  
40 ratio of 0.6, tensile breaking strain of 0.0005, and a maximum bending angle of 0.03 radians,  
41 values that were calibrated against observed fracture and calving patterns on the  
42 Greenlandic glacier Sermeq Kujalleq (Jakobshavns Isbrae). In the present study, ice strength  
43 was varied by adjusting initial damage density  $d$  from 0 (no damage) to 0.6. This damage  
44 index represents a reduction in load-bearing area and thus has a similar physical meaning to  
45 damage as commonly defined (e.g. LeMaitre, 2012; Borstad et al. 2012). However, the  
46 dependence of modelled ice properties on particle and bond parameters means that values  
47 of  $d$  are not directly comparable to damage variables used in other studies, including the  
48 BISICLES model discussed below. Ice damage typically increases during model runs as  
49 beams are broken in response to inter-particle stresses. Unlike the initial prescribed damage



50  $d$ , which is macroscopically uniform and isotropic, emergent damage is localised and  
51 anisotropic, typically taking the form of fractures and shear zones and therefore more closely  
52 similar to real damaged ice (Åström and Benn, 2019).

53 The HiDEM model domain incorporates the entire area of TEIS and extends 20 to 30 km  
54 upglacier of the grounding line. The domain is based on BedMachine v.2 (Morlighem, 2020),  
55 which incorporates the REMA ice-surface elevation DEM (Howat et al., 2019), hydrostatic ice  
56 thickness for the fully floating regions, and recent updates to the Thwaites Glacier bed and  
57 adjacent seafloor (Jordan et al., 2020). The glacier bed DEM does not incorporate recent  
58 data on the TEIS pinning point presented by Wild et al. (2021); implications of this omission  
59 are discussed below.

60 The model domain was adjusted in a short surface relaxation in Elmer/Ice, to ensure that the  
61 ice shelf base near the grounding line was at equilibrium with stresses in the ice as well as  
62 buoyant forces. Ice viscosity and basal resistance were then estimated following the serial  
63 inversion workflow described in Gladstone et al. (in prep) using MEaSURES v.2 velocity data  
64 (Rignot et al., 2011a, b; Mougnot et al., 2012, 2017). The REMA tile covering TEIS is based  
65 on data acquired in 2013-2014 and the velocity data are from 2007 and 2009. The model  
66 domain should thus be regarded as representing an approximation to conditions in recent  
67 years rather than a specific snapshot in time. Subglacial friction coefficients for grounded  
68 portions of the domain were determined assuming a linear bed friction law. Friction  
69 coefficients were converted to SI units and rescaled ( $\times 10^{-5}$ ) for use in HiDEM. Rescaling bed  
70 friction coefficients is necessary to produce useful ice-displacement magnitudes, because  
71 HiDEM simulates glacier sliding and fracture taking over timescales of seconds, whereas in  
72 reality these processes take place over timescales of hours to years (van Dongen et al.,  
73 2020).

74  
75 In the form used in this study, HiDEM is a purely brittle-elastic model and does not include  
76 viscous deformation of the ice. For simulations of short-lived calving processes it is sufficient  
77 to allow the domain to evolve under the gravitational and buoyant forces arising from ice  
78 geometry and water depth. Crevasses and rifts on ice shelves, however, typically propagate  
79 on long timescales during which ice can undergo large displacements, and for such cases  
80 some external model forcing is often desirable (e.g. Åström and Benn, 2019; Åström et al.,  
81 2021). In the runs reported here, we applied a force at the upstream boundary of the domain  
82 that produced a close approximation of the observed velocity structure near the grounding  
83 line. The simulated TEIS domain contained  $10^9$  particles and run over 36 hours using 2048  
84 cores on the Mahti supercomputer at the CSC-IT Centre for Science.

85  
86 BISICLES is a continuum ice flow model based on a vertically integrated stress balance  
87 equation (Cornford et al 2020). Its treatment of fracture processes is limited to the calculation  
88 of a scalar damage  $D(x, y, t)$ , which modifies the effective viscosity.  $D(x, y, t)$  can be  
89 calculated with a simple process model (Sun et al., 2016). That model, however, lacks the  
90 skill to simulate the observations in TEIS. Instead, we estimate  $D(x, y, t)$ , together with basal  
91 friction, through regularized optimizations conducted for monthly intervals through 2016 to  
92 2020, using velocity data derived from the Sentinel-1 imagery. The model domain covers the  
93 Amundsen Sea Embayment drainage basins including the entire Thwaites Glacier, and is  
94 based upon the BedMachine v.2 ice thickness and bedrock elevation (Morlighem, 2020).

95  
96 To assess the possible dynamic response of Thwaites Glacier to further changes on TEIS,  
97 we conducted a set of BISICLES simulations to 2100 with varying damage, ice shelf



98 thickness  $h(x, y, t)$  and pinning point friction. All simulations start with the basal friction  
99 calibrated to March 2016, which then evolves according to a regularized Coulomb law  
00 (Joughin et al., 2019, Zoet and Iverson, 2020). A simple set of calving criteria are also in play:  
01 ice is removed wherever  $(1-D)h < 5$  m or where ice speed exceeds  $10^4$  m/yr. The damage  
02 calving criterion is similar to the full-depth crevasse calving law of Nick et al. (2010), and  
03 determines the position of the ice front rather than a calving rate. Four experiments are  
04 reported here, designed to assess the impact of different physical processes. Experiment 00  
05 is a control, with  $D(x,y)$  set to the values determined for March 2016, and basal melt rates are  
06 set such that ice shelf thickness remains constant throughout. Experiment E0 aimed to  
07 determine the impact of damage evolution in isolation.  $D(x,y)$  was increased linearly within  
08 the ice shelf from 2016 to reach the value determined for March 2020, and then continued to  
09 increase at the same rate to 2026 at which point  $D(x,y) \sim 1$  across the shear zone,  
10 representing complete separation. As in 00, ice shelf thickness was held constant in time.  
11 Experiment ER includes both damage evolution and dynamic shelf-thickness evolution. In  
12 this experiment, damage was treated in the same way as E0 but the ice shelf thickness is  
13 allowed to evolve according to its velocity, without being permitted to contact the bedrock  
14 below: the grounding line may retreat but not advance. Finally, experiment UR 'unpins' TEIS,  
15 setting the ice thickness in the shear zone to zero in 2016. It allows the ice shelf to evolve in  
16 the same way as ER.

17

### 18 3. Observations

19

#### 20 3.1 Velocity structure 2015-2021

21

22 The large-scale velocity structure of TEIS underwent little change over the period 2015 to  
23 2020 (Fig. 2). On all velocity maps, ice flow vectors on to the shelf are aligned approximately  
24 normal to the general trend of the grounding line, and over most of the shelf ice progressively  
25 veer towards the north-east as ice approaches the pinning point. The only exception to this  
26 pattern is in a relatively small region west and south-west of the pinning point, where ice flow  
27 is predominantly towards the north-west. Over most of the shelf, flow speeds are typically in  
28 the range 1 to 3 m/day and an order of magnitude lower above and adjacent to the pinning  
29 point. Sustained shrinkage of the area bounded by the 0.2 m/day velocity contour indicates  
30 progressive loss of traction over the pinning point, consistent with previous work that  
31 demonstrated ongoing ice thinning in this region (Alley et al., 2021; Wild et al. 2021).

32

#### 33 3.2 Fracture and strain 2015 - 2021

34

35 Although the large-scale velocity structure of TEIS has remained relatively constant from  
36 2015 to 2020, considerable changes in fracture patterns and strain rates occurred during this  
37 period. In Sentinel-1 imagery, evidence for fracturing takes two forms: 1) broad surface  
38 troughs indicating depressions above basal crevasses, and 2) sharp-edged linear features  
39 indicating surface crevasses or full-depth rifts (e.g. Luckman et al., 2012). In the earliest  
40 Sentinel-1 images (2014), sets of sub-parallel basal crevasses occur down-flow of the  
41 grounding line and up-flow of the pinning point (Fig. 3). The latter set extends diagonally  
42 across the shelf from south-west to north-east, coincident with the transition between rapidly  
43 and slowly moving ice shown in Figure 2. This region is interpreted as a narrow shear zone  
44 (S: Fig. 3; Alley et al., 2021) between slowly-moving ice over the pinning point (P) and more  
45 rapidly-flowing ice on the main part of the shelf, hereafter termed the *TEIS shear zone*. In late  
46 2016 and early 2017, a set of secondary basal crevasses started to develop at a high angle  
47 to the TEIS shear zone, on the upglacier (southern) side (T: Fig. 3). These subsequently  
propagated southward across the shelf and increased in number. During 2017, the  
easternmost of these secondary crevasses developed into a full-depth rift, visible as a sharp-



48 edged feature on the Sentinel imagery and leading to the detachment of a tabular berg ~18  
49 km long and up to 2 km wide (C1, Fig. 3). Other areas of active calving are evident on both  
50 the eastern (C2) and western (C3) flanks of TEIS, the latter releasing tabular bergs into the  
51 area formerly occupied by the shear margin between TEIS and TWIT. Evidence for full-depth  
52 rifting within the TEIS shear zone was initially confined to short wing cracks across blocks  
53 bounded by basal crevasses, but became increasingly widespread through time.

54  
55 Rapid evolution of the shear zone since 2018 is further illustrated by velocity gradients and  
56 patterns of shear strain (Figs. 4 and 5). In 2018, a narrow band of high strain existed in the  
57 northeastern portion of the shear zone, while strain in the remainder of the shear zone was  
58 lower in magnitude and distributed over a much wider area. In late 2020, a second narrow  
59 shear band appeared at the south-west end of the TEIS shear zone, then both bands  
60 connected and extended across the full extent of the shelf by early 2021, indicating a  
61 transition to full-thickness fracture. Velocity gradients across the south-western half of the  
62 shear zone (Fig. 5) show distributed strain in the first quarter of 2020, suggesting  
63 predominantly viscous deformation or strain distributed across numerous fractures. During  
64 2020 all velocity profiles show increasing localization of strain as the shear zone transitioned  
65 to full-depth fracture. Increasing shear localization is accompanied by an increase in ice  
66 velocity on the upglacier side of the shear zone and a decrease on the downglacier (pinning  
67 point) side. On the upglacier side, ice acceleration is substantial and ongoing (Fig. 6), with  
68 >40% increase in ice speed in the central part of TEIS between 2018 and 2021.

69

### 70 **3.3 Long-term perspective: Velocity and strain from MODIS data 2002 - 2021**

71 The shear zone on TEIS was already a well-established feature in 2014, when the Sentinel-1  
72 data begins. Evolution of TEIS prior to 2014, and the possible origin of the shear zone, can be  
73 inferred using MODIS and other historical data (Alley et al., 2021). These data are at a lower  
74 spatial resolution (500 m) than the Sentinel-1 imagery, and strain rates were calculated over  
75 a longer length scale (2500 m). This precludes detailed analysis, but the MODIS data provide  
76 a valuable record of large-scale patterns of velocity and strain and their changes through  
77 time.

78

79 Figure 6 shows a time series of velocity in the central part of TEIS, c. 15 km upglacier of the  
80 pinning point (magenta circle on Fig. 4). The ice accelerated between 2002 and 2006, then  
81 rapidly decreased to a minimum in 2009 before gradually increasing until 2020 when the current  
82 quasi-exponential acceleration began. The 2002-2006 acceleration is attributed to strong  
83 coupling between TEIS and TWIT (Alley et al., 2021). Thwaites Western Ice Tongue increased in  
84 speed after 2002 (Miles et al., 2020), possibly in response to progressive unpinning (Tinto and  
85 Bell, 2011), and the strong shear margin between the two portions of the shelf allowed TEIS to be  
86 dragged forward (Alley et al., 2021). After 2006, the shear margin between TEIS and TWIT  
87 fragmented and weakened, reducing coupling and allowing TEIS to decelerate. Meanwhile, TWIT  
88 fragmented, transitioned into a 'mélange ice shelf' and continued to accelerate (Miles et al., 2020;  
89 Alley et al., 2021).

90

91 Patterns of strain on TEIS for three key time periods are shown in Figure 7. During the TEIS  
92 acceleration event (2005 - 2006), a band of positive (dextral; blue) shear strain outlines the shear  
93 margin between TEIS and TWIT, while a zone of negative (sinistral; red) shear is evident around  
94 the locus of the modern TEIS shear zone. Very high compressive longitudinal strain rates  
95 upstream of the TEIS pinning point indicate significant backstress during the acceleration event.  
96 After the acceleration event (2009-2010), the shear margin between TEIS and TWIT weakened  
97 (Lhermitte et al., 2020; Alley et al., 2021), reducing the coupling between TEIS and TWIT, and  
98 allowing TEIS to slow down again. This appears in the middle column of Fig. 7, where high shear



99 strain rates delimit the weakened shear margin between TEIS and TWIT. In contrast, both shear  
100 strain and longitudinal strain rates are very low upstream of the TEIS pinning point. However, the  
101 first large fractures within the TEIS shear zone are visible in the MODIS imagery (marked with an  
102 arrow). Data for 2019-2020 show a renewed increase of shear strain in the vicinity of the TEIS  
103 shear zone and the development of extensive rifting. This phase of shear zone evolution has  
104 been discussed in detail above (Figs. 4 & 5).

105

106 In summary, TEIS has undergone a process of fragmentation in the last five years, including  
107 brittle failure along a major shear zone up-glacier of the pinning point, formation of tensile cracks  
108 on the main body of the shelf, and release of tabular bergs on both eastern and western flanks of  
109 TEIS. This pattern of failure is consistent with longitudinal (flow-parallel) compression and  
110 transverse extension of the shelf. The origins of the TEIS shear zone can be traced at least to the  
111 2002 - 2006 acceleration event on TEIS, when zones of high longitudinal and shear strain  
112 developed upglacier of the pinning point, indicating high backstress at that time. Fragmentation of  
113 the shelf increased since 2014, with increasing shear localization and extensive full-thickness  
114 rifting since late 2020. Weakening of the shear zone has been accompanied by rapid (possibly  
115 exponential) acceleration of the ice on the upglacier side.

116

## 117 4. Modelling

118

### 119 4.1 Fracture modelling with HiDEM

120 Experiments with HiDEM were designed to test two hypotheses on the causes of the observed  
121 fragmentation of TEIS: 1) fragmentation is related to a reduction of backstress on the shelf,  
122 consequent upon progressive unpinning; and 2) fragmentation is related to progressive  
123 weakening of the ice and continuing backstress from the pinning point. To test these hypotheses,  
124 we conducted a matrix of runs with different combinations of friction over the pinning point and  
125 ice damage density. The results show that widespread fracturing of the shelf does not occur in  
126 runs with low damage density ( $d < 0.3$ ) but does occur for runs with high damage density ( $d =$   
127  $0.6$ ). Results from two runs with  $d = 0.6$  and different pinning point friction are presented here.

128

129 Results for  $d = 0.6$  and pinning point friction coefficients rescaled from the Elmer/Ice inversion  
130 (hereafter: *baseline friction*) are shown in Figure 8. The pinning point does not exert any  
131 significant influence on the pattern of ice displacement, and ice is able to slide over the proximal  
132 side of the submarine ridge then calves at its crest. Extensive rifting and calving occurs on the  
133 eastern flank of TEIS (highlighted by discontinuities in displacement magnitudes), but only limited  
134 fracturing occurs on the western flank.

135

136 Figure 9 shows results for  $d = 0.6$  and a no slip boundary condition over the pinning point. In this  
137 case, a teardrop-shaped area of stagnant, largely intact ice extends upglacier from the pinning  
138 point. Patterns of ice displacement on TEIS show progressive veering towards the north-east as  
139 it approaches the stagnant zone. Mobile and stagnant ice are separated by a shear zone,  
140 indicated by the sharp discontinuity in displacement magnitudes. The east and west flanks of  
141 TEIS exhibit widespread propagation of subparallel rifts and calving of tabular icebergs and  
142 tensile fractures are developed in the central part of the shelf (Fig. 10). Unlike the separate linear  
143 fractures observed on TEIS, the tensile fractures are part of stepped features with both shear and  
144 tensile components. This difference probably reflect the lack of viscous processes in the model.

145

146 The fracture pattern in the 'no slip' simulation thus exhibits many similarities with that observed in  
147 February 2021 (cf. Figs. 1 & 10). Key common features are: 1) a triangular zone of slowly moving  
148 or stagnant ice extending upglacier from the pinning point; 2) deflection of ice flow around the  
149 stagnant zone; 3) development of a shear zone (TEIS shear zone) upglacier of the pinning point;  
150 4) and rifting and calving along the eastern and western flanks of TEIS. The close similarity



51 between the observed pattern of fracture and the 'no slip' HiDEM simulation support the  
52 conclusion that the recent fragmentation of TEIS occurred in response to uniaxial compression  
53 (i.e. opposing driving stress and backstress from the pinning point) and absence of transverse  
54 confining pressure.

55

#### 56 **4.2 BISICLES model results: damage evolution and future dynamics**

57 An initial set of simulations with BISICLES was conducted to optimize basal traction and  
58 damage  $D$ , using monthly velocity data for the period 2016 and 2020. Results for the month  
59 of March are shown in Figure 11. Model speeds match observed speeds across the majority  
60 of Thwaites Glacier: the notable exception is TWIT, where brittle fracture and the formation of  
61 a mélange shelf are poorly described by the continuum model. There the mismatch is as  
62 much as 1.3 m/day, or 10% of the observed speed. The observed increase in speed in TEIS  
63 between 2016 and 2020 can be reproduced in the model by minor changes in the basal  
64 traction and by a strip of damage coincident with the shear zone adjacent to the pinning point  
65 whose magnitude increases over time.

66

67 We then used the optimized basal traction and damage values in March 2016 as the starting  
68 point for forward model simulations (Fig. 12). In all cases, quite large changes occur to the  
69 velocity pattern on TEIS. Experiment 00 (control experiment with damage and ice shelf  
70 thickness held constant at March 2016 values) exhibits a reduction in speed of ~0.5 m/day  
71 across both ice shelf regions and immediately upstream by 2032, caused by the thinning of  
72 the ice upstream and the resulting reduced gravitational driving stress. Experiment E0  
73 (linearly extrapolated damage, constant ice shelf thickness) produces an increase in speed  
74 on TEIS upglacier of the pinning point, attributed to reduced ability of the shelf to support  
75 backstress. In contrast, ice around the grounding line of TWIT and the eastern grounding line  
76 of TEIS decreases in speed, for similar reasons to that in the control experiment. Experiment  
77 ER (extrapolated damage, dynamically evolving ice shelf thickness) results in faster flow over  
78 most of TEIS, with the ice shelf acceleration leading to thinning and a further loss of  
79 buttressing. The greatest speed increase is seen in experiment UR, because here resistive  
80 stresses are reduced as in ER and the shelf also becomes unconfined on the western flank.  
81 In all cases, there is at most modest increase in the ice flux across grounding line onto TEIS,  
82 even when large acceleration occurs on the shelf. This is consistent with inversion results  
83 that indicate that at the present time, backstress from TEIS does not make a significant  
84 contribution to the force balance along much of the grounding line.

85

86 The future contribution of Thwaites Glacier to sea level rise computed by the BISICLES  
87 model depends only weakly on changes in TEIS. Figure 13 shows the discharge of ice above  
88 flotation, that is  $V = \int_{\Omega_G} \vec{\nabla}_H \cdot (\vec{u} (h - h_f)) d\Omega_G$ , where  $\vec{u}$  is the horizontal ice velocity,  $h$  is ice  
89 thickness,  $h_f$  is the flotation thickness,  $\vec{\nabla}_H$  is the horizontal gradient operator, and  $\Omega_G$  is the  
90 grounded part of the Thwaites drainage basin. Although the models with extrapolated  
91 damage and evolving ice thickness do exhibit greater discharge over the first few years, all  
92 four experiments show the same long-term trend, tending toward a common equilibrium. The  
93 brief spikes in discharge evident in experiments 00 and E0 have nothing to do with the ice  
94 shelves: instead, the artificial maintenance of ice shelf thickness the region to the west of the  
95 ice shelves result in large ice speeds and a (modelled) calving event that reduces basal  
96 traction in a region clearly visible in Figure 11.

97

98

99



00 **5. Discussion**

01

02 **5.1 Observed and modelled fracturing**

03 Sentinel-1 data, available since 2014, show that TEIS has transitioned from a largely intact ice  
04 shelf into an extensively fractured state, with full-depth fracturing along the TEIS shear zone,  
05 rifting and tabular calving along both eastern and western flanks, tensile fracturing in the central  
06 part of the shelf, and acceleration of ice flow. Concurrently, ice has been progressively  
07 decoupling from the submarine pinning point at its distal end.

08

09 The HiDEM modelling highlights the key role of backstress from the pinning point in this pattern  
10 of fracturing. The TEIS shear zone does not develop in runs where friction over the pinning point  
11 has the baseline values derived by rescaling output from the Elmer/Ice inversion. In contrast, a  
12 shear zone and other features similar to the observed fracture pattern do develop in runs where a  
13 no-slip boundary condition is imposed over the pinning point. It may appear paradoxical that the  
14 shear zone fails to develop under model boundary conditions derived from observed ice  
15 geometry and dynamics. Two reasons may be suggested for this.

16

17 First, the inversion-derived friction coefficients over the pinning point may be unrepresentative  
18 because of uncertainties associated with the sea-floor topography, the inversion process in  
19 Elmer/Ice, and the subsequent rescaling for HiDEM. Radar data show the bedrock topography is  
20 up to 200 m shallower than indicated by the gravity inversion used as the basis for the model bed  
21 (Wild et al., 2021). In the Elmer/Ice inversion, the small area of the pinning point may mean that  
22 the inverted basal resistance is too low as the result of spatial smoothing in the regularization  
23 process. Rescaling of friction to account for the different functional timescales of HiDEM and  
24 Elmer/Ice introduces further uncertainties, particularly because HiDEM does not incorporate  
25 viscous processes. Taken together, these factors could mean that the bed is 'too slippery' over the  
26 pinning point in the HiDEM simulations using the baseline friction values.

27

28 Second, the necessity for high pinning point friction to create a shear zone in HiDEM may mean  
29 that the observed TEIS shear zone was initiated at a time when pinning point friction was greater  
30 than it was when the model input data were acquired (2007 and 2009 for MEaSURES and 2013-  
31 2014 for REMA). It is therefore possible that the TEIS shear zone developed when the pinning  
32 point provided greater backstress, and that progressive weakening through shear localisation and  
33 damage evolution has allowed the shear zone to persist although pinning point friction has been  
34 diminishing. Whatever the case, the HiDEM results are unequivocal: the observed fracture  
35 pattern requires backstress from the pinning point sufficient to initiate and sustain shear failure  
36 in the shelf. That is, backstress must consistently exceed the evolving effective strength of  
37 TEIS.

38

39 In the HiDEM runs, a high initial damage density ( $d = 0.6$ ) is required to produce a shear zone.  
40 This does not imply that a similar degree of pervasive damage was required to initiate the TEIS  
41 shear zone. As noted above, the properties of ice in HiDEM reflect a range of parameters and we  
42 chose damage density as a transparent and easily tunable control on ice strength. It must also be  
43 emphasised that the version of HiDEM used here is purely brittle-elastic, and does not  
44 incorporate viscous deformation. This means that the model cannot include processes likely to  
45 have been important on TEIS, particularly viscous shear localisation in the early development of  
46 the shear zone. In addition, evolution of TEIS likely involved a number of factors not included in  
47 the simulations, such as stress concentrations associated with basal roughness elements such  
48 as advected crevasses and basal channels.

49

50

51



## 52 **5.2 Causes of fragmentation of TEIS**

53 The transformation of TEIS from a largely intact ice shelf into its currently fragmented state  
54 suggests the pinning point has shifted from being a stabilising to a destabilising influence.  
55 Formerly, backstress from the pinning point was sufficient to constrain ice flow, but  
56 insufficient to initiate fracturing. At some point the balance shifted, such that backstress from  
57 the pinning point exceeded the effective strength of the ice, and damage was able to  
58 accumulate. This shift may have occurred for three fundamental reasons:

- 59
- 60 1. Changes in resistive stresses at the grounded margins of the shelf;
- 61
- 62 2. Changes in stress patterns due to interactions between TEIS and TWIT; and
- 63
- 64 3. Changes to the effective strength of the shelf.
- 65

66 The grounded margins of TEIS have undergone overall retreat in recent decades. The area  
67 of ice-bed contact at the TEIS pinning point has reduced (Wild et al., 2021), and the  
68 grounding line at the upglacier boundary of TEIS has retreated (e.g. Rignot et al., 2014;  
69 Milillo et al., 2019). In addition, interferograms of TEIS for the 1990s indicate the presence of  
70 a possible additional pinning point in the middle of TEIS (Rignot, 2001), which is not evident  
71 in more recent times. While reduction in the area of the TEIS pinning point may be expected  
72 to have reduced backstress on the shelf, the other changes may have increased longitudinal  
73 compressive stresses on the floating ice.

74

75 Concomitant with the changes to grounded margins, there have been large changes in the  
76 relationship between TEIS and TWIT. First, acceleration of TWIT after 2002 (itself likely a  
77 response to weakening of a sub-shelf pinning point) was transmitted across shear margin to  
78 TEIS, causing the observed speed-up between 2002 and 2006 (**Fig. 6**). This speed-up was  
79 associated with increased longitudinal and shear strain on TEIS, indicating increased loading  
80 on the shelf. Subsequently, fragmentation and opening of the shear margin exposed the  
81 western flank of TEIS, reducing lateral confining stress on that side.

82

83 Several factors may have contributed to weakening TEIS in recent decades. Basal melting in  
84 response to incursions of warm, deep water has reduced ice-shelf thickness, with basal melt  
85 rates typically on the order of 5 m/yr (Seroussi et al. 2017; Wåhlin et al., 2021; Alley et al.,  
86 2021). Focused basal melting in sub-shelf channels can increase basal roughness, create  
87 local stress concentrations and interact with fracture processes. Weakening may also occur  
88 through the advection of damage from upglacier, and basal crevasses or other fractures  
89 could seed additional damage when they reach different stress regimes. Finally, damage can  
90 accumulate through time via positive feedbacks between damage and strain (Åström and  
91 Benn, 2019; Lhermitte et al., 2020).

92

93 The recent evolution of TEIS may have involved a combination of all the above factors. On  
94 the balance of available evidence, we propose the following sequence of events as the most  
95 likely cause of the recent fragmentation. The TEIS shear zone was initiated, or was  
96 significantly modified, in the mid-2000s, when TEIS accelerated in response to stresses  
97 transferred across the strong shear margin with TWIT (Alley et al. 2021). During the  
98 acceleration event, high longitudinal and shear strain rates developed on TEIS in response to  
99 elevated longitudinal compression supported by backstress from the pinning point. Large  
00 fractures within the TEIS shear zone first appear in satellite imagery after the acceleration  
01 event, suggesting that damage was initiated or increased in response to elevated stresses



02 (Fig. 7). Fragmentation, opening and significant weakening of the shear margin between  
03 TEIS and TWIT removed confining pressure from the western flank of TEIS, encouraging  
04 transverse extension in response to ongoing longitudinal compression. Concurrently, damage  
05 on the shelf continued to accumulate due to positive feedbacks between damage and strain,  
06 and basal melting reduced ice-shelf thickness and possibly contributed to weakening the TEIS  
07 shear zone (Wählin et al., 2021). Sentinel-1 data show increasing development of tensile  
08 fractures since 2017 in response to transverse extension (Fig. 3), and increasing  
09 concentration of strain and extensive rifting within the TEIS shear zone since 2020 (Fig. 5).  
10 Thus, although backstress from the pinning point has likely diminished through time (Wild et  
11 al., 2021), accumulation of damage on TEIS has ensured that the ice in the shear zone has  
12 remained the weakest link in the system. Fragmentation of TEIS was not a consequence of  
13 unpinning; on the contrary, fragmentation reflects stresses originating at the pinning point  
14 acting on progressively weakening ice.

15

16 Backstress from the pinning point, once a crucial source of support for TEIS, is now hastening its  
17 destruction. Complete fragmentation of TEIS appears to be imminent and disintegration could  
18 occur sooner than the ~10 year timescale implied by rates of thinning and unpinning (cf. Wild et  
19 al., 2021). Complete loss of the shelf may follow, although the former pinning point and fast ice  
20 may retard the evacuation of icebergs in much the same way as currently observed on TWIT.

21

### 22 **5.3 Future implications of TEIS loss**

23 The BISICLES model results indicate that loss of strength in the shear zone or unpinning of  
24 TEIS will likely have little impact on basin-wide discharge from Thwaites Glacier. There is  
25 currently no evidence that the imminent loss of TEIS will hasten marine ice sheet instability or  
26 the demise of Thwaites Glacier. However, future evolution of Thwaites may be significantly  
27 influenced by calving processes along unbuttressed grounding lines, and it is possible that  
28 calving and iceberg overturn may increase, perhaps substantially, if the ice shelves are lost.

29

30 Water depths along the grounding line of TEIS are currently in the range 400 - 700 m, which is  
31 below the likely threshold for ice-cliff instability (cf. Bassis and Walker, 2012; Crawford et al.,  
32 2020). The glacier bed deepens substantially 40 km upglacier of the current grounding line and  
33 Thwaites Glacier may enter the MICI regime if the ice front retreats to that point. Until then, ice  
34 retreat will involve calving by processes such as melt-undercutting, longitudinal extension and  
35 buoyant calving (e.g. Benn et al., 2007; Benn and Åström, 2019). Detailed observations and  
36 process modelling will be required to understand how ice shelf removal will affect calving  
37 processes and ice-retreat rates in this region (e.g. Winberry et al., 2020; Crawford et al., 2020).

38

### 39 **5.4 The destabilising role of pinning points in ice shelf loss**

40 Observations of Antarctic ice shelf disintegration have implicated two main mechanisms for ice  
41 shelf collapse: hydrofracture and unpinning from bedrock features (e.g. Doake et al., 1998;  
42 Scambos et al., 2003). In the context of ice-shelf collapse, hydrofracturing requires a combination  
43 of surface meltwater and stressed ice. By offsetting the effects of lithostatic pressure, water in  
44 surface crevasses can shift an ice shelf into a tensile stress regime, leading to deep penetration  
45 of the crevasses and runaway failure (Scambos et al., 2003; Robel and Banwell, 2019; Lai et  
46 al., 2020). Supraglacial stream networks can transport water off ice shelves or focus it in  
47 vulnerable areas, and hence play either a stabilising or destabilising role in the hydrofracture  
48 process (Kingslake et al., 2017; Bell et al., 2017; Dell et al., 2020). Alternatively, unpinning  
49 from ice shelf margins or grounding points impacts ice shelf stability by removing sources of  
50 resistive stress. Unpinning can occur in response to increased basal melting, accumulation of  
51 damage, or other factors including reduction of landfast sea ice (Doake et al., 1998; Glasser and  
52 Scambos, 2008; Lhermitte et al., 2020). Some ice-shelf break-up events involve a combination of



53 unpinning and hydrofracture (e.g. Larsen B: Doake et al., 1998; Scambos et al., 2003), while  
54 other cases indicate that unpinning can lead to ice-shelf fragmentation in the absence of surface  
55 melt (e.g. TWIT: Miles et al., 2019).

56  
57 Our results indicate that a third mechanism, failure of ice triggered by backstress from a pinning  
58 point, can also lead to ice-shelf fragmentation. We propose the term *backstress-triggered failure*  
59 for this mechanism. The contrast between backstress-triggered failure and unpinning is  
60 instructive. Pinning points are sources of resistive stress that oppose gravitational driving  
61 stresses. In structurally intact ice shelves, the opposition of resistive stress and driving stress is  
62 manifest as compressive membrane stresses, including across-flow oriented 'compressive  
63 arches' and upflow oriented backstress (Doake et al., 1998; van der Veen, 2013). Removal or  
64 weakening of a pinning point (complete or partial unpinning) breaks the symmetry between  
65 resistive and driving stress, removes or reduces the associated compressive membrane  
66 stresses, and renders the ice vulnerable to *failure in tension*. In contrast, during backstress-  
67 triggered failure the resistive stress - driving stress opposition remains in place, but instead of  
68 supporting membrane stresses the ice *fails in compression*. The fundamental difference between  
69 the unpinning and backstress-triggered failure scenarios is the location of the weakest link in the  
70 system: in the former it is the contact between the shelf and the pinning point, in the latter it is the  
71 ice itself. Pinning points and promontories at the margins of ice shelves are known to serve as  
72 nucleation points for fractures (e.g. Arndt et al., 2018; De Rydt et al., 2019), but pinning points  
73 generally act as stabilizing features (e.g. Favier et al., 2016; Still et al., 2019). On TEIS, the  
74 switch from pinning-point enabled stability to backstress-triggered failure occurred as a  
75 consequence of a number of factors, including interactions between TEIS and TWIT, removal of  
76 lateral confining pressure, shelf thinning from basal melting, and positive feedbacks between  
77 damage and strain. Similar factors may also prove a lethal combination on other ice shelves.

78  
79 On ice shelves in steady state, pinning points play a crucial role in their stability and in  
80 buttressing the upstream flow of ice off the Antarctic continent. If increasing basal melt and/or  
81 changing flow dynamics upset this balance, stresses are likely to concentrate upstream of  
82 pinning points, causing irreversible damage. In most circumstances, pinning points are essential  
83 for ice shelf stability, but as ice shelves thin and weaken, pinning points can plant the seeds of  
84 their demise.

#### 85 86 **Code and data availability**

87  
88 Data sources are cited in the text. Code for HiDEM, Elmer/Ice and BISICLES is open-source and  
89 freely available.

#### 90 91 **Author contributions**

92  
93 DB and AL designed and oversaw the study in discussion with JB and EP; remote sensing  
94 analyses were conducted by AL (Sentinel-1), SB (DEMs) and KA (MODIS); computer modelling  
95 was done by JÅ and AC (HiDEM), RG, AC and TZ (Elmer/Ice) and SC (BISICLES). DB wrote the  
96 manuscript with input from all authors.

#### 97 98 **Competing interests**

99  
00 The authors declare that they have no conflict of interest.

#### 01 02 **Acknowledgements**

03  
04 This work is from the DOMINOS and TARSAN projects, components of the International



05 Thwaites Glacier Collaboration (ITGC). Funding was provided by the National Science  
06 Foundation (NSF: Grants 1738896 and 1929991) and Natural Environment Research Council  
07 (NERC: Grant NE/S006605/1). Rupert Gladstone is supported by Academy of Finland grant  
08 number 322430, Thomas Zwinger by grant number 322978. Logistics provided by NSF-U.S.  
09 Antarctic Program and NERC-British Antarctic Survey. Sentinel-1 data were provided by the  
10 Copernicus Program of the European Commission. ITGC contribution number ITGC-XXX.

11

12

### 13 References

14

15 Alley, K.E., Wild, C.T., Luckman, A., Scambos, T.A., Truffer, M., Pettit, E.C., Muto, A., Wallin, B.,  
16 Klinger, M., Sutterley, T. and Child, S.F., 2021. Two decades of dynamic change and progressive  
17 destabilization on the Thwaites Eastern Ice Shelf. *The Cryosphere Discussions*, 1-31.

18

19 Arndt, J.E., Larter, R.D., Friedl, P., Gohl, K. and Höppner, K., 2018. Bathymetric controls on calving processes  
20 at Pine Island Glacier. *The Cryosphere*, 12(6), 2039-2050.

21

22 Åström, J.A. and Benn, D.I., 2019. Effective rheology across the fragmentation transition for sea ice  
23 and ice shelves. *Geophysical Research Letters*, 46(22), 13099-13106.

24

25 Åström, J.A., Riikilä, T.I., Tallinen, T., Zwinger, T., Benn, D., Moore, J.C. and Timonen, J., 2013. A  
26 particle based simulation model for glacier dynamics. *The Cryosphere*, 7(5), 1591-1602.

27

28 Åström, J., Cook, S., Enderlin, E.M., Sutherland, D.A., Mazur, A. and Glasser, N., 2021.  
29 Fragmentation theory reveals processes controlling iceberg size distributions. *Journal of Glaciology*  
30 67 (264), 603-612.

31

32 Bell, R.E., Chu, W., Kingslake, J., Das, I., Tedesco, M., Tinto, K.J., Zappa, C.J., Frezzotti, M.,  
33 Boghosian, A. and Lee, W.S., 2017. Antarctic ice shelf potentially stabilized by export of meltwater in  
34 surface river. *Nature*, 544(7650), 344-348.

35

36 Borstad, C.P., Khazendar, A., Larour, E., Morlighem, M., Rignot, E., Schodlok, M.P. and Seroussi, H.,  
37 2012. A damage mechanics assessment of the Larsen B ice shelf prior to collapse: Toward a  
38 physically-based calving law. *Geophysical Research Letters*, 39, L18502,

39

doi:10.1029/2012GL053317.

40

41 Cook, A.J. and Vaughan, D.G., 2010. Overview of areal changes of the ice shelves on the Antarctic  
42 Peninsula over the past 50 years. *The Cryosphere*, 4(1), 77-98.

43

44 Cornford, S.L., Seroussi, H., Asay-Davis, X.S., Gudmundsson, G.H., Arthern, R., Borstad, C.,  
45 Christmann, J., Dias dos Santos, T., Feldmann, J., Goldberg, D. and Hoffman, M.J., 2020. Results of  
46 the third Marine Ice Sheet Model Intercomparison Project (MISMIP+). *The Cryosphere*, 14(7), 2283-  
47 2301.

48

49 Crawford, A.J., Benn, D.I., Todd, J., Åström, J.A., Bassis, J.N. and Zwinger, T. 2021. Marine ice-cliff  
50 instability modelling shows mixed-mode ice-cliff failure and yields calving rate parameterization.  
51 *Nature Communications* 12(1), 1-9. doi: 10.1038/s41467-021-23070-7

52

53 DeConto, R.M., Pollard, D., Alley, R.B., Velicogna, I., Gasson, E., Gomez, N., Sadai, S., Condrón, A.,  
54 Gilford, D.M., Ashe, E.L. and Kopp, R.E., 2021. The Paris Climate Agreement and future sea-level  
55 rise from Antarctica. *Nature*, 593(7857), 83-89.

56

57 Dell, R., Arnold, N., Willis, I., Banwell, A., Williamson, A., Pritchard, H. and Orr, A., 2020. Lateral  
58 meltwater transfer across an Antarctic ice shelf. *The Cryosphere*, 14(7), 2313-2330.



- 59  
60 De Rydt, J., Gudmundsson, G.H., Nagler, T. and Wuite, J., 2019. Calving cycle of the Brunt Ice Shelf,  
61 Antarctica, driven by changes in ice shelf geometry. *The Cryosphere*, 13(10), pp.2771-2787.  
62  
63 Doake, C.S.M., Corr, H.F.J., Rott, H., Skvarca, P. and Young, N.W., 1998. Breakup and conditions for  
64 stability of the northern Larsen Ice Shelf, Antarctica. *Nature*, 391(6669), 778-780.  
65  
66 Dupont, T.K. and Alley, R.B., 2005. Assessment of the importance of ice-shelf buttressing to ice-sheet  
67 flow. *Geophysical Research Letters*, 32(4), L04503, doi:10.1029/2004GL022024.  
68  
69 Favier, L., Pattyn, F., Berger, S., and Drews, R.: Dynamic influence of pinning points on marine ice-  
70 sheet stability: a numerical study in Dronning Maud Land, East Antarctica, *The Cryosphere*, 10,  
71 2623–2635, <https://doi.org/10.5194/tc-10-2623-2016>
- 72 Fox-Kemper, B., H. T. Hewitt, C. Xiao, G. Aðalgeirsdóttir, S. S. Drijfhout, T. L. Edwards, N. R.  
73 Golledge, M. Hemer, R. E. Kopp, G. Krinner, A. Mix, D. Notz, S. Nowicki, I. S. Nurhati, L. Ruiz, J-B.  
74 Sallée, A. B. A. Slangen, Y. Yu, 2021, Ocean, Cryosphere and Sea Level Change. In: *Climate*  
75 *Change 2021: The Physical Science Basis. Contribution of Working Group I to the Sixth Assessment*  
76 *Report of the Intergovernmental Panel on Climate Change* [Masson-Delmotte, V., P. Zhai, A. Pirani,  
77 S. L. Connors, C. Péan, S. Berger, N. Caud, Y. Chen, L. Goldfarb, M. I. Gomis, M. Huang, K. Leitzell,  
78 E. Lonnoy, J.B.R. Matthews, T. K. Maycock, T. Waterfield, O. Yelekçi, R. Yu and B. Zhou (eds.)].  
79 Cambridge University Press.
- 80 Fretwell, P., Pritchard, H.D., Vaughan, D.G., Bamber, J.L., Barrand, N.E., Bell, R., Bianchi, C.,  
81 Bingham, R.G., Blankenship, D.D., Casassa, G., Catania, G., Callens, D., Conway, H., Cook, A.J.,  
82 Corr, H.F.J., Damaske, D., Damm, V., Ferraccioli, F., Forsberg, R., Fujita, S., Gim, Y., Gogineni, P.,  
83 Griggs, J.A., Hindmarsh, R.C.A., Holmlund, P., Holt, J.W., Jacobel, R.W., Jenkins, A., Jokat, W.,  
84 Jordan, T., King, E.C., Kohler, J., Krabill, W., Riger-Kusk, M., Langle, K.A., Leitchenkov, G.,  
85 Leuschen, C., Luyendyk, B.P., Matsuoka, K., Mouginot, J., Nitsche, F.O., Nogi, Y., Nost, O.A., Popov,  
86 S.V., Rignot, E., Rippon, D.M., Rivera, A., Roberts, J., Ross, N., Siegert, M.J., Smith, A.M., Steinhage,  
87 D., Studinger, M., Sun, B., Tinto, B.K., Welch, B.C., Wilson, D., Young, D.A., Xiangbin, C., Zirizzotti,  
88 A., 2013. Bedmap2: improved ice bed, surface and thickness datasets for Antarctica. *The Cryosphere*  
89 7, 375–393. <https://doi.org/10.5194/tc-7-375-2013>
- 90 Gardner, A. S., M. A. Fahnestock, and T. A. Scambos, 2019 [update to time of data download]:  
91 ITS\_LIVE Regional Glacier and Ice Sheet Surface Velocities. Data archived at National Snow and Ice  
92 Data Center; doi:10.5067/6II6VW8LLWJ7.
- 93 Glasser, N.F. and Scambos, T.A., 2008. A structural glaciological analysis of the 2002 Larsen B  
94 ice-shelf collapse. *Journal of Glaciology*, 54(184), 3-16.  
95  
96 Howat, I.M., Porter, C., Smith, B.E., Noh, M.J. and Morin, P., 2019. The reference elevation model  
97 of Antarctica. *The Cryosphere*, 13(2), 665-674.  
98  
99 Jordan, T.A., Porter, D., Tinto, K., Millan, R., Muto, A., Hogan, K., Larter, R.D., Graham, A.G. and  
00 Paden, J.D., 2020. New gravity-derived bathymetry for the Thwaites, Crosson, and Dotson ice  
01 shelves revealing two ice shelf populations. *The Cryosphere*, 14(9), 2869-2882.  
02  
03 Lai, C.Y., Kingslake, J., Wearing, M.G., Chen, P.H.C., Gentine, P., Li, H., Spergel, J.J. and van  
04 Wessel, J.M., 2020. Vulnerability of Antarctica's ice shelves to meltwater-driven  
05 fracture. *Nature*, 584(7822), 574-578.  
06  
07 Lemaitre, J., 2012. *A course on damage mechanics*. Springer Science & Business Media.  
08



- 09 Lhermitte, S., Sun, S., Shuman, C., Wouters, B., Pattyn, F., Wuite, J., Berthier, E. and Nagler, T.,  
10 2020. Damage accelerates ice shelf instability and mass loss in Amundsen Sea  
11 Embayment. *Proceedings of the National Academy of Sciences*, 117(40), 24735-24741.  
12
- 13 Liu, Y., Moore, J.C., Cheng, X., Gladstone, R.M., Bassis, J.N., Liu, H., Wen, J. and Hui, F., 2015.  
14 Ocean-driven thinning enhances iceberg calving and retreat of Antarctic ice shelves. *Proceedings of  
15 the National Academy of Sciences*, 112(11), 3263-3268.  
16
- 17 Luckman, A., Jansen, D., Kulesa, B., King, E.C., Sammonds, P. and Benn, D.I., 2012. Basal  
18 crevasses in Larsen C Ice Shelf and implications for their global abundance. *The Cryosphere*, 6(1),  
19 113-123.  
20
- 21 Luckman, A., Benn, D. I., Cottier, F., Bevan, S., Nilsen, F., Inall, M., 2015. Calving rates at tidewater  
22 glaciers vary strongly with ocean temperature. *Nature Communications* 6, 8566+.  
23 <http://dx.doi.org/10.1038/ncomms9566>  
24
- 25 Miles, B.W.J., Stokes, C.R., Jenkins, A., Jordan, J.R., Jamieson, S.S.R. and Gudmundsson, G.H.,  
26 2020. Intermittent structural weakening and acceleration of the Thwaites Glacier Tongue between  
27 2000 and 2018. *Journal of Glaciology*, 66(257), 485-495.
- 28 P. Milillo, E. Rignot, P. Rizzoli, B. Scheuchl, J. Mouginot, J. Bueso-Bello, P. Prats-Iraola,  
29 Heterogeneous retreat and ice melt of Thwaites Glacier, West Antarctica. *Science Advances* 5,  
30 eaau3433 (2019).
- 31 Mouginot, J., Scheuchl, B., Rignot, E., 2012. Mapping of Ice Motion in Antarctica Using Synthetic-  
32 Aperture Radar Data. *Remote Sensing* 4, 2753–2767. <https://doi.org/10.3390/rs4092753>  
33
- 34 Mouginot, J., Scheuchl, B. and Rignot, E. 2017. *MEaSURES Annual Antarctic Ice Velocity Maps  
35 2005-2017, Version 1*. [Indicate subset used]. Boulder, Colorado USA. NASA National Snow and Ice  
36 Data Center Distributed Active Archive Center. doi: <https://doi.org/10.5067/9T4EPQXTJYW9>.  
37 [Accessed 2020].  
38
- 39 Morlighem, M., Rignot, E., Binder, T., Blankenship, D., Drews, R., Eagles, G., Eisen, O., Ferraccioli,  
40 F., Forsberg, R., Fretwell, P. and Goel, V., 2020. Deep glacial troughs and stabilizing ridges unveiled  
41 beneath the margins of the Antarctic ice sheet. *Nature Geoscience*, 13(2), 132-137.  
42
- 43 Nick, F.M., Van der Veen, C.J., Vieli, A. and Benn, D.I., 2010. A physically based calving model  
44 applied to marine outlet glaciers and implications for the glacier dynamics. *Journal of  
45 Glaciology*, 56(199), 781-794.  
46
- 47 Pollard, D., DeConto, R.M. and Alley, R.B., 2015. Potential Antarctic Ice Sheet retreat driven by  
48 hydrofracturing and ice cliff failure. *Earth and Planetary Science Letters*, 412, 112-121.
- 49 Rignot, E. 2001. Evidence for rapid retreat and mass loss of Thwaites Glacier, West Antarctica.  
50 *Journal of Glaciology* 47 (157), 213-222.
- 51 Rignot, E., Mouginot, J., Scheuchl, B., 2011a. MEaSURES InSAR-Based Antarctica Ice Velocity Map.  
52 Boulder, Colorado, USA: NASA DAAC at the National Snow and Ice Data Center.  
53 <https://doi.org/10.5067/MEASURES/CRYOSPHERE/nsidc-0484.001> [Accessed 2020]  
54
- 55 Rignot, E., Mouginot, J., Scheuchl, B., 2011b. Ice Flow of the Antarctic Ice Sheet. *Science* 333, 1427–  
56 1430. <https://doi.org/10.1126/science.1208336>  
57

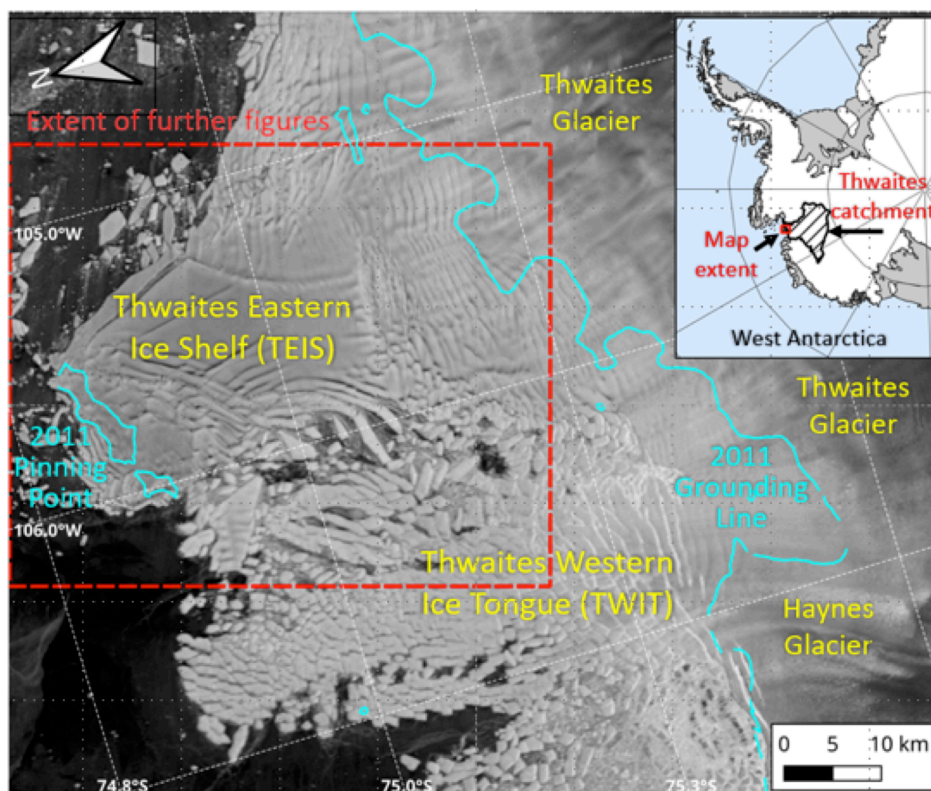


- 58 Rignot, E., Mouginot, J., Morlighem, M., Seroussi, H., Scheuchl, B., 2014. Widespread, rapid  
59 grounding line retreat of Pine Island, Thwaites, Smith, and Kohler glaciers, West Antarctica, from  
60 1992 to 2011. *Geophysical Research Letters* 41, 3502–3509. <https://doi.org/10.1002/2014GL060140>  
61
- 62 Robel, A.A. and Banwell, A.F., 2019. A speed limit on ice shelf collapse through  
63 hydrofracture. *Geophysical Research Letters*, 46(21), 12092-12100.  
64
- 65 Scambos, T., Hulbe, C. and Fahnestock, M., 2003. Climate-induced ice shelf disintegration in the  
66 Antarctic Peninsula. *Antarctic Peninsula Climate Variability: Historical and Paleoenvironmental*  
67 *Perspectives, Antarct. Res. Ser.*, 79, 79-92.  
68
- 69 Scambos, T.A., Bohlander, J.A., Shuman, C.A. and Skvarca, P., 2004. Glacier acceleration and  
70 thinning after ice shelf collapse in the Larsen B embayment, Antarctica. *Geophysical Research*  
71 *Letters*, 31(18).  
72
- 73 Scambos, T.A., Bell, R.E., Alley, R.B., Anandakrishnan, S., Bromwich, D.H., Brunt, K., Christianson,  
74 K., Creyts, T., Das, S.B., DeConto, R. and Dutrieux, P., 2017. How much, how fast?: A science  
75 review and outlook for research on the instability of Antarctica's Thwaites Glacier in the 21st  
76 century. *Global and Planetary Change*, 153,16-34.  
77
- 78 Schoof, C., 2012. Marine ice sheet stability. *Journal of Fluid Mechanics*, 698, 62-72.  
79
- 80 Seroussi, H., Nakayama, Y., Larour, E., Menemenlis, D., Morlighem, M., Rignot, E. and Khazendar,  
81 A., 2017. Continued retreat of Thwaites Glacier, West Antarctica, controlled by bed topography and  
82 ocean circulation. *Geophysical Research Letters*, 44(12), 6191-6199.  
83
- 84 Still, H., Campbell, A. and Hulbe, C., 2019. Mechanical analysis of pinning points in the Ross Ice  
85 Shelf, Antarctica. *Annals of Glaciology*, 60(78), pp.32-41.  
86
- 87 Sun, S., Cornford, S.L., Moore, J.C., Gladstone, R. and Zhao, L., 2017. Ice shelf fracture  
88 parameterization in an ice sheet model. *The Cryosphere*, 11(6), 2543-2554.  
89
- 90 Sun, S., Pattyn, F., Simon, E.G., Albrecht, T., Cornford, S., Calov, R., Dumas, C., Gillet-Chaulet, F.,  
91 Goelzer, H., Golledge, N.R. and Greve, R., 2020. Antarctic ice sheet response to sudden and  
92 sustained ice-shelf collapse (ABUMIP). *Journal of Glaciology*, 66(260), 891-904.  
93
- 94 Tinto, K.J. and Bell, R.E., 2011. Progressive unpinning of Thwaites Glacier from newly identified  
95 offshore ridge: Constraints from aerogravity. *Geophysical Research Letters*, 38(20), L20503,  
96 [doi:10.1029/2011GL049026](https://doi.org/10.1029/2011GL049026),  
97
- 98 Van der Veen, C.J., 2013. *Fundamentals of glacier dynamics, Second edition*. CRC press.  
99
- 00 van Dongen, E. C. H., Åström, J.A., Jouvét, G., Todd, J., Benn, D.I. and Funk, M., 2020. Numerical  
01 modeling shows increased fracturing due to melt-undercutting prior to major calving at Bowdoin  
02 Glacier. *Frontiers in Earth Science* 8.  
03
- 04 Wählin, A.K., Graham, A.G.C., Hogan, K.A., Queste, B.Y., Boehme, L., Larter, R.D., Pettit, E.C.,  
05 Wellner, J. and Heywood, K.J., 2021. Pathways and modification of warm water flowing beneath  
06 Thwaites Ice Shelf, West Antarctica. *Science Advances*, 7(15), p.eabd7254.  
07
- 08 Wild, C.T., Alley, K.E., Muto, A., Truffer, M., Scambos, T.A. and Pettit, E.C., 2021. Weakening of the  
09 pinning point buttressing Thwaites Glacier, West Antarctica. *The Cryosphere Discussions*, 1-28.  
10



12 **Figures**

13

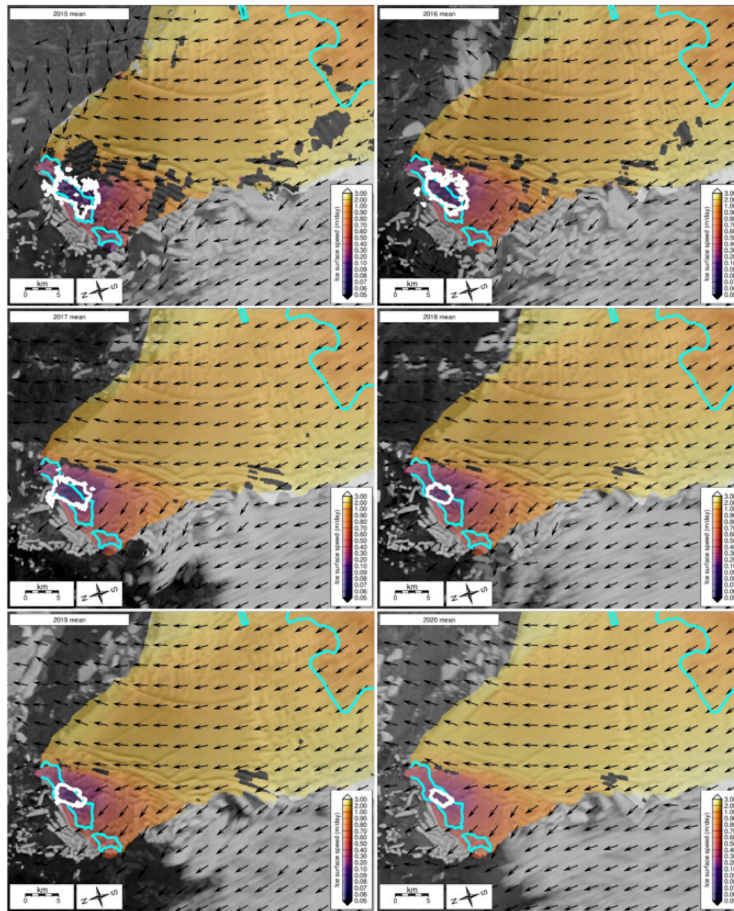


14

15

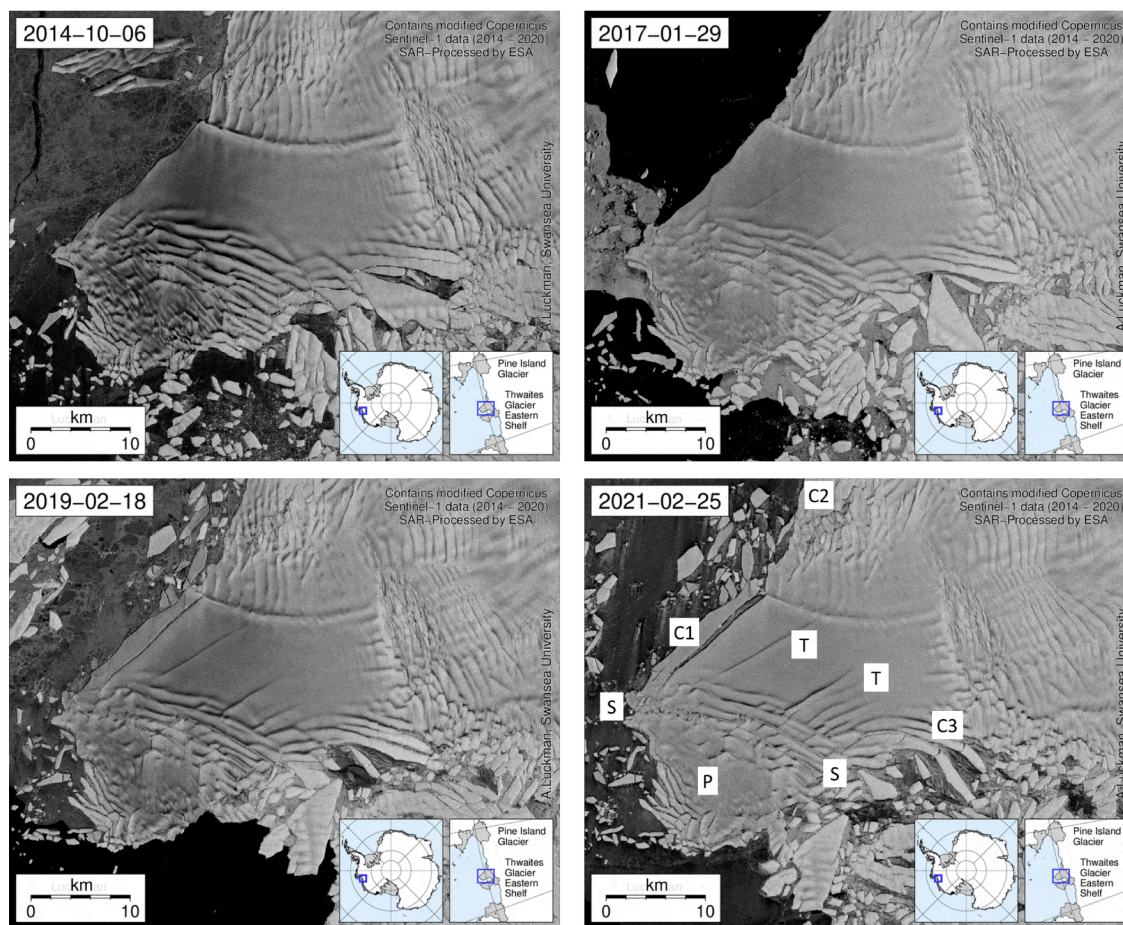
16 **Figure 1:** The floating extensions of Thwaites Glacier, showing location of the Eastern Ice  
17 Shelf (TEIS) the Western Ice Tongue (TWIT) and the position of grounding lines and the  
18 location of pinning points in 2011 from Rignot et al. (2014). Image based on modified  
19 Copernicus Sentinel-1 data (2014-2021), SAR-processed by ESA.

20



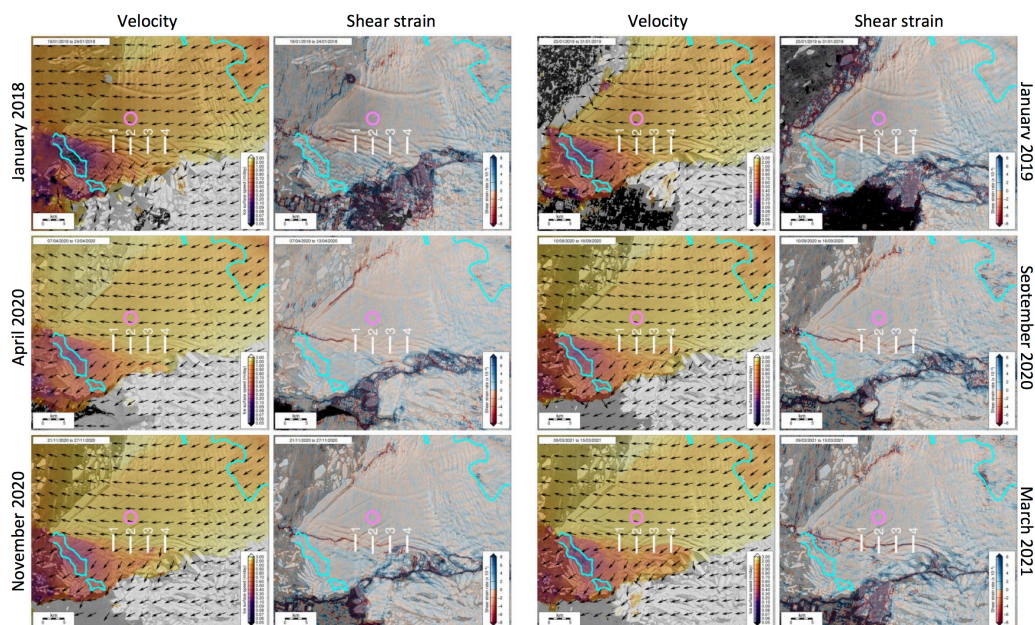
21  
22

23 **Figure 2:** Time series of mean annual velocity on TEIS derived from Sentinel-1 speckle-  
24 tracking between 2015 and 2020. Arrows show flow direction. Cyan lines are MEaSUREs  
25 InSAR-derived grounding lines from 2011 (Rignot et al., 2014). White lines delineate the 0.2  
26 m/day velocity contour which is centred on the pinning point. Images contain modified  
27 Copernicus Sentinel-1 data (2014-2021), SAR-processed by ESA.



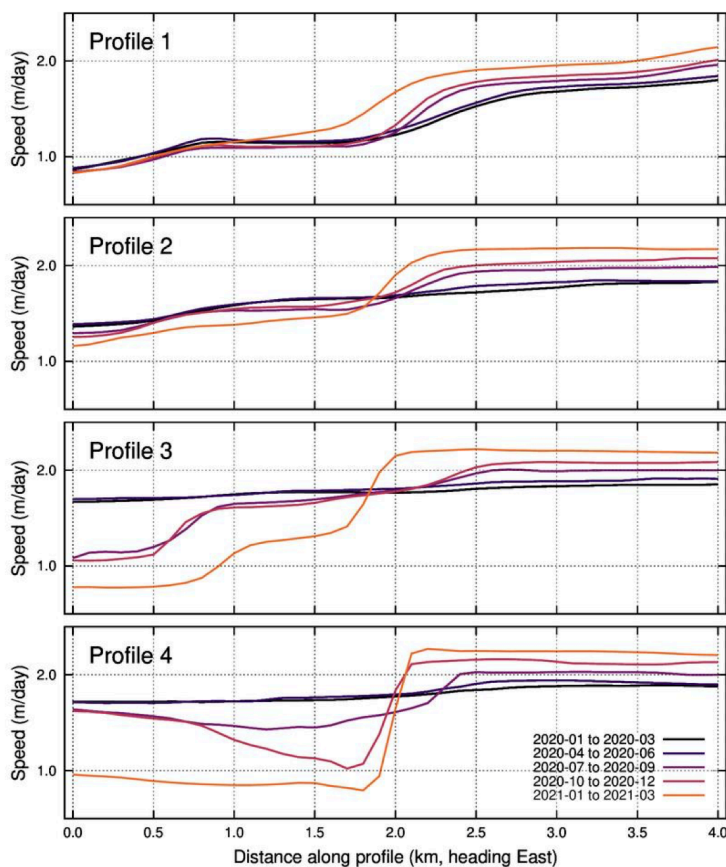
28  
29  
30  
31  
32  
33  
34

**Figure 3:** Fracture patterns on Thwaites Eastern Ice Shelf (TEIS) 2014 - 2021. The final frame labels key features described in the text: S - S: TEIS shear zone; T: tensile cracks; C1 - C3: calving along rifts; P: slow-moving, relatively intact ice above pinning point. Images contain modified Copernicus Sentinel-1 data (2014-2021), SAR-processed by ESA.



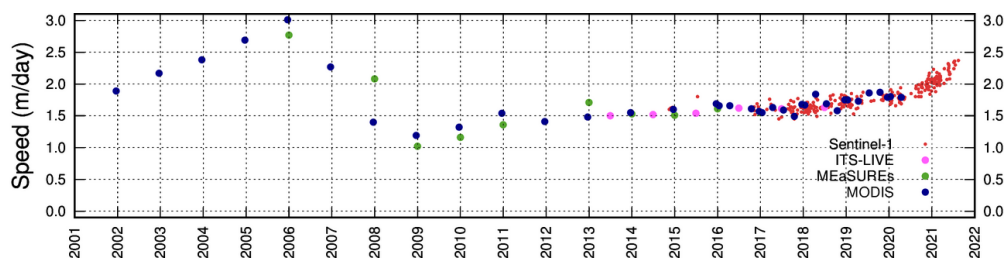
35  
36  
37  
38  
39  
40  
41  
42  
43  
44  
45

**Figure 4:** Evolution of velocity (first and third columns) and shear strain (second and fourth columns) on TEIS derived from Sentinel-1 speckle-tracking between 2016 and 2021. Specific image pairs are chosen for excellent coherence and minimal noise, and to focus on recent months. Cyan lines are MEaSURES InSAR-derived grounding lines from 2011 showing the location of historic known pinning points. White lines show positions of numbered profiles used to extract velocities presented in **Figure 5**. The magenta circle indicates the location of the velocity time series shown in **Figure 6**. Images contain modified Copernicus Sentinel-1 data (2014-2021), SAR-processed by ESA.



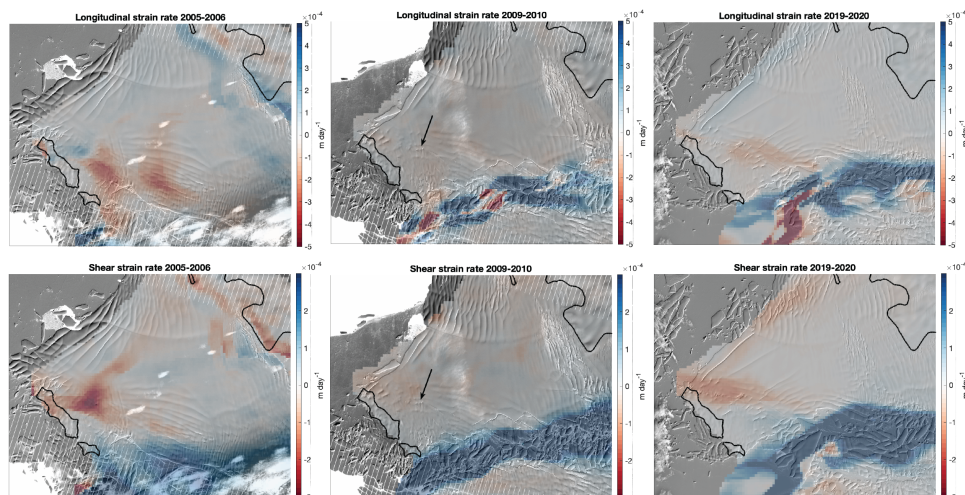
46  
 47  
 48  
 49  
 50  
 51

**Figure 5:** Profiles of mean quarterly surface velocity during 2020 and 2021 from Sentinel-1 speckle/feature tracking along the white lines shown in Fig. 4.



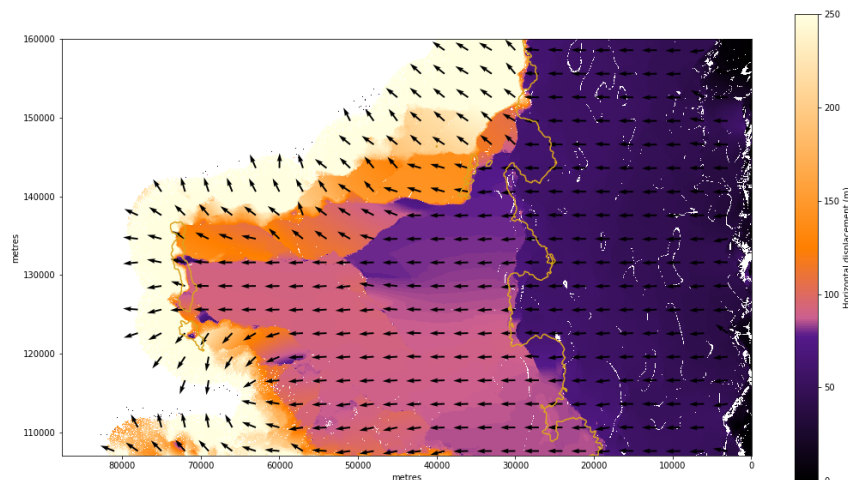
52  
 53  
 54  
 55  
 56  
 57  
 58  
 59

**Figure 6:** Velocity evolution at a point in the centre of TEIS from MODIS (blue dots; Alley et al., 2021), ITS\_LIVE (pink), MEaSUREs (green) and Sentinel-1 (red) showing the 2002-2006 acceleration, the 2006-2008 slowdown, 2008-2020 modest acceleration and recent rapid acceleration as the shelf crossed the fracture transition. Location of velocity data is shown by the magenta circle in Figure 4.



60  
61  
62  
63  
64  
65  
66  
67  
68  
69  
70  
71  
72

**Figure 7:** Mean longitudinal strain rates (top row) and shear strain rates (bottom row), in 2005-2006 during the TEIS acceleration event (left-hand column), 2009-2010 (middle column), and 2019-2020 (right-hand column). The TEIS-TWIT shear margin is near the bottom of each image and the TEIS shear zone is to the right of the twin 'islands' of the pinning point, outlined in black. Crevasses in the location of the current shear zone are indicated by the arrow in the middle column. Landsat-7 (first and second column) and Landsat-8 (third column) imagery courtesy of the U.S. Geological Survey. Strain rates are from Alley et al. (2021).

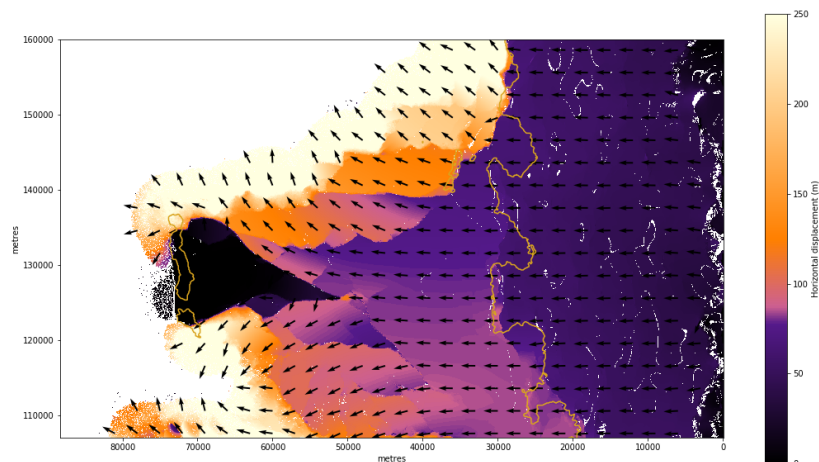


73  
74  
75  
76

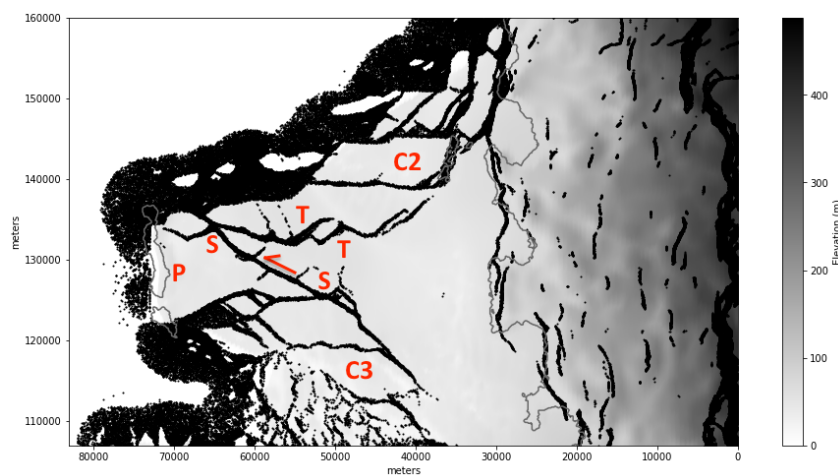
**Figure 8:** Ice displacement pattern simulated in HiDEM model run with the baseline friction boundary condition over the pinning point (i.e. values derived from the Elmer/Ice inversion



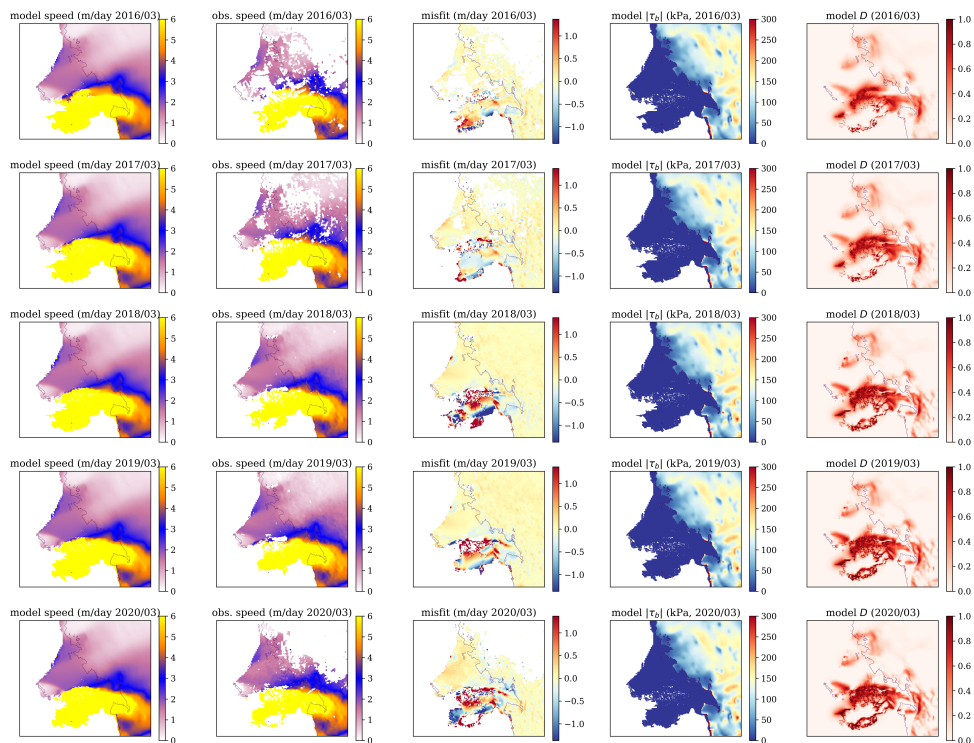
77 rescaled for HiDEM) and damage density = 0.6. Grounding lines are indicated by orange  
78 lines. The observed shear zone (cf. **Fig. 3**) does not develop in this simulation. The zone of  
79 large displacements around TEIS (yellow) consists of calved icebergs.  
80



81  
82  
83 **Figure 9:** Pattern of ice displacement simulated in HiDEM model run with a no-slip boundary  
84 condition over the pinning point and damage density = 0.6. Note the triangular area of  
85 stationary ice extending upglacier from the pinning point, and the sharp displacement  
86 gradient (shear zone) between it and the main body of TEIS.  
87



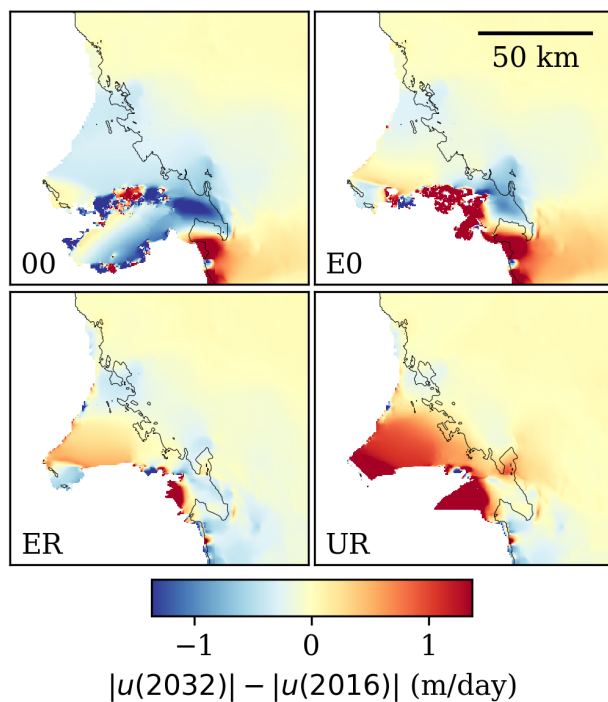
88  
89 **Figure 10:** Fracture pattern simulated in HiDEM for the no-slip boundary condition over the  
90 pinning point and damage density = 0.6. Bonds broken during the simulation are indicated in  
91 black, surface elevation in greyscale shading, and grounded areas delineated by grey lines.  
92 Letters indicate features analogous to the observed features in **Fig. 3**; P: pinning point; S:  
93 shear zone; C2, C3: ripping and calving on the eastern and western flanks; and T: tensile  
94 cracks.  
95  
96



97

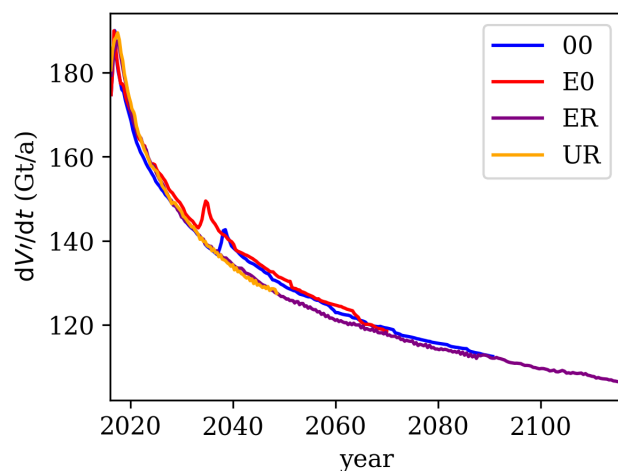
98

99 **Figure 11:** BISICLES inverse problem results, March 2016-2020. The first and second  
00 columns show the optimized model velocities and observed velocities; the third column  
01 shows the misfit between modelled and observed velocities; and the fourth and fifth columns  
02 show the resulting optimized basal traction and damage. Each row shows data for March of  
03 one year.



04  
05  
06  
07  
08

**Figure 12:** Output of BISICLES simulations of TEIS, showing differences in velocity relative to 2016. For details of each run, see text.



09  
10  
11  
12  
13

**Figure 13:** Discharge of ice above flotation  $V$  associated with modelled changes to TEIS.